Double beta decay of ^{96}Zr

R. Arnold [k], C. Augier [i], J. Baker [e], A. Barabash [1,h], D. Blum [i], V. Brudanin [c],
A.J. Caffrey [e], J.E. Campagne [i], E. Caurier [k], D. Dassié [a], V. Egorov [c],
T. Filipova [c,i], R. Gurriaran [a], J.L. Guyonnet [k], F. Hubert [a], Ph. Hubert [a],
S. Jullian [i], I. Kisel [c], O. Kochetov [c], V.N. Kornoukhov [h], V. Kovalenko [c],
D. Lalanne [i], F. Laplanche [i], F. Leccia [a], I. Linck [k], C. Longuemare [b],
Ch. Marquet [a], F. Mauger [b], H.W. Nicholson [j], I. Pilugin [h], F. Piquemal [a],
J-L. Reyss [d], X. Sarazin [i], F. Scheibling [k], J. Suhonen [f], C.S. Sutton [j],
G. Szklarz [i], V. Timkin [c], R. Torres [a], V.I. Tretyak [g], V. Umatov [h],
I. Vanyushin [h], A. Vareille [a], Yu. Vasilyev [g], Ts. Vylov [c]

[a] *CENBG, IN2P3-CNRS et Université de Bordeaux, 33170 Gradignan, France*
[b] *LPC, IN2P3-CNRS et Université de Caen, 14032 Caen, France*
[c] *JINR, 141980 Dubna, Russian Federation*
[d] *CFR, CNRS, 91190 Gif sur Yvette, France*
[e] *INEL, Idaho Falls, ID 83415, USA*
[f] *JYVÄSKYLÄ University, 40351 Jyväskylä, Finland*
[g] *INR, 252028 Kiev, Ukraine*
[h] *ITEP, 117259 Moscow, Russian Federation*
[i] *LAL, IN2P3-CNRS et Université Paris-Sud, 91405 Orsay, France*
[j] *MHC, South Hadley, Massachusetts 01075, USA*
[k] *IReS, IN2P3-CNRS et Université Louis Pasteur, 67037 Strasbourg, France*

Abstract

After 10357 h of running the NEMO-2 tracking detector with an isotopically enriched zirconium source (0.084 mol yr of ^{96}Zr), a $\beta\beta2\nu$ decay half-life of $T_{1/2} = (2.1^{+0.8(\text{stat})}_{-0.4(\text{stat})} \pm 0.2(\text{syst})) \cdot 10^{19}$ y was measured. Limits with a 90% C.L. on the ^{96}Zr half-lives of $1.0 \cdot 10^{21}$ y for $\beta\beta0\nu$ decay to the ground state, $3.9 \cdot 10^{20}$ y to the 2^+ excited state and $3.5 \cdot 10^{20}$ y for $\beta\beta0\nu\chi^0$ decay with a Majoron (χ^0) were obtained. The data also provide direct limits at the 90% C.L. for the ^{94}Zr half-lives. These limits are $1.1 \cdot 10^{17}$ y for $\beta\beta2\nu$ decay to the ground state, $1.9 \cdot 10^{19}$ y

[1] Corresponding author, Institute of Theoretical and Experimental Physics, B. Cheremushkinskaya 25, 117259 Moscow, Russian Federation.

for $\beta\beta 0\nu$ decay to the ground state and $2.3 \cdot 10^{18}$ y for $\beta\beta 0\nu\chi^0$ decay to ground state. © 1999 Published by Elsevier Science B.V. All rights reserved.

1. Introduction

Neutrinoless double beta decay ($\beta\beta 0\nu$) is one of the best probes for physics beyond the standard model of electroweak interactions. Its existence is tied to fundamental aspects of particle physics such as lepton number nonconservation, neutrino mass, right-handed currents in the electroweak interaction, a massless Goldstone boson (Majoron), the structure of the Higgs' sector and supersymmetry. To date, only lower limits on half-lives ($T_{1/2}^{0\nu}$) of different nuclei have been obtained experimentally. These limits are used to deduce upper limits on the Majorana neutrino mass, the right-handed-current admixture parameter, the Majoron–Majorana neutrino coupling constant, etc. [1–4]. One particular source of uncertainty in the above analysis is the evaluation of the nuclear matrix elements entering the theoretical expressions for these fundamental observables. In connection with the $\beta\beta 0\nu$ decay, the detection of double beta decay with the emission of two neutrinos ($\beta\beta 2\nu$), which is an allowed process of second order in the Standard Model, enables the experimental determination of nuclear matrix elements involved in the double beta decay processes. This, in turn, leads to the development of theoretical schemes for nuclear matrix-element calculations, both in connection with the $\beta\beta 2\nu$ decays as well as the $\beta\beta 0\nu$ decays. More exact calculations of nuclear matrix elements allow a less ambiguous extraction of the values of the relevant $\beta\beta 0\nu$ observables mentioned above.

The NEMO Collaboration has started to build the tracking detector NEMO-3 [5], which will be capable of studying $\beta\beta 0\nu$ decays of ^{100}Mo and other nuclei up to half-lives of $\sim 10^{25}$ y, this corresponds to a Majorana neutrino mass of ~ 0.1–0.3 eV. The sensitivity to $\beta\beta 0\nu\chi^0$ and $\beta\beta 2\nu$ decays will be of order 10^{23} y and 10^{22} y, respectively. Two prototype detectors, NEMO-1 [6] and NEMO-2 [7] were constructed as research and development tools to establish reliable techniques. The NEMO-2 detector, designed for $\beta\beta$ background studies and $\beta\beta 2\nu$ decay, operated in the Fréjus Underground Laboratory (4800 m w.e.) from 1991 to 1997. During this period the $\beta\beta 2\nu$ decays of ^{100}Mo [8], ^{116}Cd [9], ^{82}Se [10] and ^{96}Zr were investigated in detail through measurements of the summed electron energy spectra, angular distributions and single electron spectra. Enriched and natural sources of zirconium were installed in the NEMO-2 detector in the autumn of 1995 together with selenium sources. Preliminary results were published in Ref. [11]. Presented here are the final results of measurements (10357 h) with ^{96}Zr, which is one of the most favourable double beta decay nuclides ($Q_{\beta\beta} = 3350$ keV). Limits on the $\beta\beta$ processes in ^{94}Zr are also given.

2. NEMO-2 detector

The NEMO-2 detector (Fig. 1) consists of a 1 m^3 tracking volume filled with helium gas and 4% ethyl alcohol. Vertically bisecting the detector is the plane of the source foil
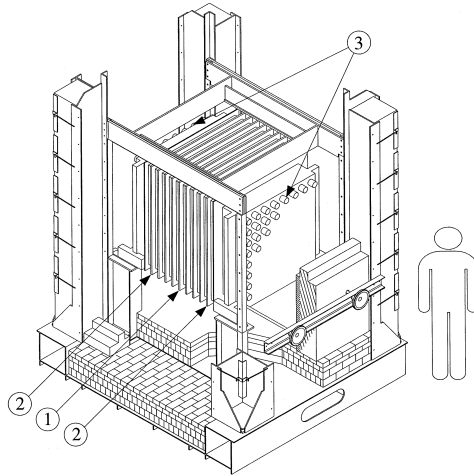
Fig. 1. The NEMO-2 detector without shielding. (1) Central frame with the source plane capable of supporting plural source foils. (2) Tracking device of 10 frames, each consisting of two perpendicular planes of 32 Geiger cells. (3) Two scintillator arrays each consisting of 5 by 5 counters. In the earlier experiment with molybdenum sources the scintillator arrays were 8 by 8 counters as depicted here.

(1 m × 1 m). Tracking is accomplished with long open Geiger cells with an octagonal cross section defined by 100 μm nickel wires. On each side of the source foil there are 10 planes of 32 cells which alternate between vertical and horizontal orientations. Collectively the cells provide three-dimensional tracking of charged particles.

A calorimeter made of scintillators covers two vertical opposing sides of the tracking volume. It consists of two planes of 25 scintillators (19 cm × 19 cm × 10 cm) combined with low radioactivity photomultipliers tubes (PMT). The tracking volume and scintillators are surrounded with a lead (5 cm) and iron (20 cm) shield.

2.1. Performance

Details of the performances and parameters are described elsewhere [7–10] while the most salient characteristics are briefly outlined here. Three-dimensional measurements of charged particle tracks are provided by the array of Geiger cells. The transverse position is given by the drift time and the longitudinal position by the plasma propagation times. The transverse resolution is 500 μm and the longitudinal resolution is 4.7 mm. Track reconstruction is accomplished with the tracking method based on the Kalman filter [12] used in the $\beta\beta$ decay analysis of the ^{100}Mo and ^{116}Cd with NEMO-2. The calorimeter energy resolution (FWHM) is 18% at 1 MeV with a time resolution of 275 ps (550 ps at 0.2 MeV). A laser and fiber optics device is used to check the stability of the scintillation detectors.

A trigger requiring two scintillation counters and four Geiger frames normally runs at a rate of 0.01–0.04 Hz depending on the radon levels in the laboratory. This trigger rate is too low for an efficient survey of the experiment, so a second trigger requiring only one counter with an energy greater than 1.3 MeV was added.

2.2. Event definition

An electron is defined by a track linking the source foil and one scintillator. The maximum scattering angle along the track has to be less than 20° to reject hard scattering situations. A photon is recognized as one or two adjacent fired scintillators without an associated particle track. For photons and electrons an energy deposited greater than 200 keV is required in order to obtain sufficiently good time resolution. The two-electron events are defined by two tracks which have a common vertex and are associated with two fired scintillators with a deposited energy of at least 200 keV in each one. A cut on the angle between the two electron tracks, $\cos(\theta_{ee}) \le 0.6$, is applied as explained in the section devoted to the results. In the analysis a two-electron event is
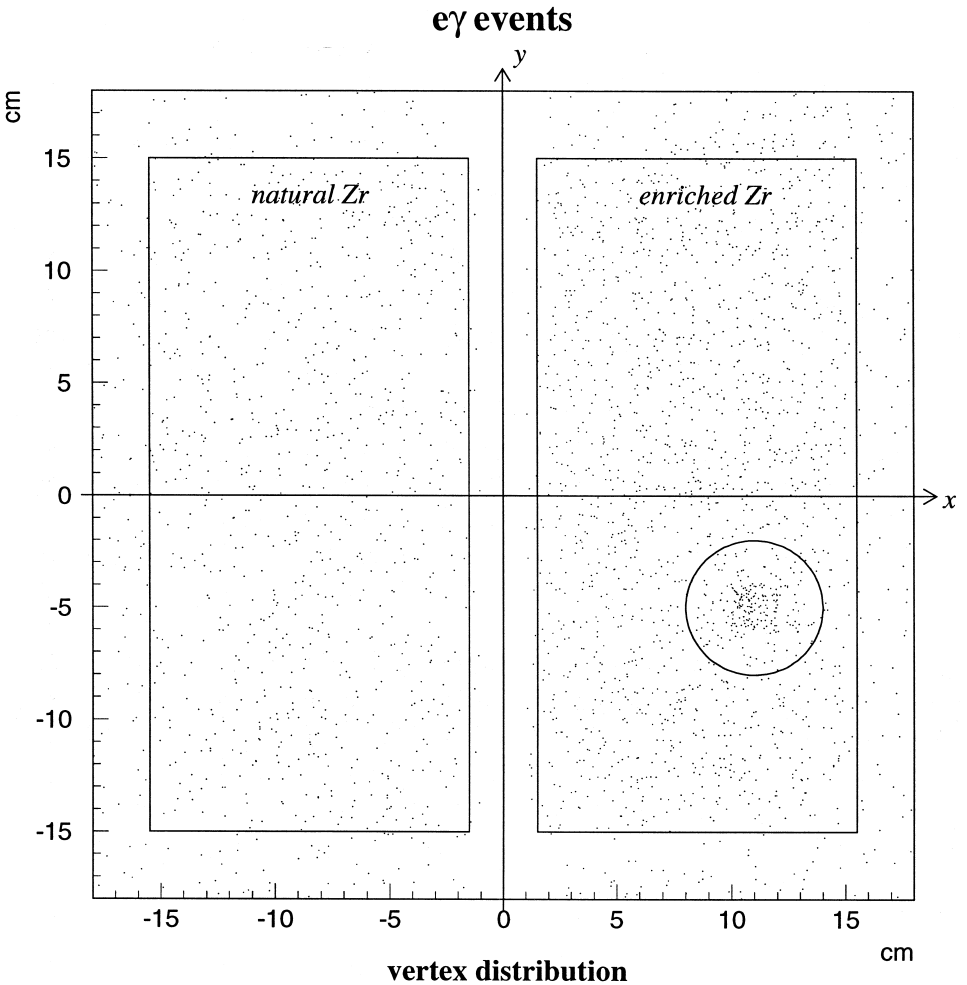

Fig. 2. Vertex position of $e\gamma$ events in the natural and enriched sources is displayed in the figure. The ''hot'' spot inside the circle is removed in the analysis.

Table 1
Radioactive contamination measurements of natural and enriched zirconium foils with HPGe detectors. Results are given in mBq/kg, upper limits are at the 90% C.L. The ''hot'' spot was cut out from the enriched zirconium foil in the measurement marked by * (see text).

Nucleus	Natural Zr		Enriched Zr	
	Jul. 1995	Oct. 1997	Jul. 1995	Oct. 1997 *
^{40}K	< 200	< 135	1083 ± 217	1133 ± 117
^{60}Co	< 10	< 4	< 17	< 5
^{137}Cs	12 ± 7	12 ± 6	73 ± 15	92 ± 8
^{152}Eu	< 16	204 ± 16	70 ± 20	153 ± 21
^{154}Eu	< 11	< 10	50 ± 10	< 36
^{208}Tl	< 8	< 5	< 15	25 ± 3
^{212}Bi	< 15	< 12	< 22	72 ± 12
^{228}Ac	< 25	< 21	90 ± 25	92 ± 13
^{214}Bi	< 13	< 12	< 13	< 15
^{234m}Pa	< 180	< 140	< 283	< 240

identified as (2e), an electron–photon event as (eγ). A more detailed description of the analysis can be found in Refs. [7–10].

2.3. Zirconium source

The zirconium source was composed of strips which were produced using a special technique that deposited zirconium oxide with binder on mylar films. The source was divided into two halves. The first half was a 20.5 g isotopically enriched zirconium foil (the ^{96}Zr enrichment is 57%) with 6.8 g of ^{96}Zr. The second half was an 18.3 g foil with natural zirconium, of which 2.80% is ^{96}Zr (0.3 g of ^{96}Zr) and 17.38% is ^{94}Zr (1.9 g of ^{94}Zr). The thickness of the foils was 50 mg/cm^2 for the enriched and 45 mg/cm^2 for the natural one. The source occupied the central portion of the source plane. The central portion was surrounded by selenium samples [10].

In the coordinate system of the detector (Fig. 2) the origin of the axes is at the center of the source plane with the x axis being horizontal and the y axis vertical. The enriched zirconium foil has positive x coordinates.

Radioactive impurities in both foils were measured twice with HPGe detectors in the Fréjus Underground Laboratory, once before their installation in the NEMO-2 detector and then after dismounting (Table 1).these two measurements can be explained if there was contamination introduced during the production and the installation of the sources into the NEMO-2 detector (see discussion in Section 3.1).

Values of the different contaminations in both foils were also obtained with the NEMO-2 detector by analyzing electron–gamma and single electron events, as explained in the sections devoted to backgrounds. A ''hot'' spot was found in the enriched zirconium foil (Fig. 2). Its characteristics are discussed below.

3. Backgrounds

In the NEMO-2 experiments, events connected with natural samples are used to estimate background events in enriched samples. In the case of the Zr sources there was

a large amount of radioactive contamination in both foils which needed to be taken into account. Backgrounds for the NEMO-2 detector had both ''internal'' and ''external'' origins.

The ''external'' background is due to photons originating from outside of the tracking detector and interacting with the source foils or with the scintillators. Compton electrons produced in the scintillators and crossing the tracking device are rejected by time-of-flight analysis. Compton electrons produced in the source foils can generate a secondary electron by the Möller scattering. A double Compton effect or pair production can also occur. These 2e background events cannot be rejected by time-of-flight cuts. The dominant contribution to the external background comes from the flux of photons emitted by radon located between the tracking detector and the shielding. Another source of background is due to the flux of photons emitted by the low background PMTs [7,9,10].

Radioactive pollution in the source foils produces a background identified as ''internal''. An electron which gives rise to the Möller effect, or is associated with an internal conversion electron, or a Compton electron can produce 2e background events.

Most of background 2e events are due to double Compton or knocked Möller electrons and have small angles between the two electrons. On the contrary, electrons in the $\beta\beta2\nu$ decay move predominantly in opposite directions. To improve the signal-to-background ratio a cut on the angle between two electrons, $\cos(\theta_{ee}) < 0.6$, is applied for the selection of 2e events as it was in the previous measurements with ^{116}Cd [9] and ^{82}Se [10].

All the Monte Carlo simulations were done with the GEANT 3.21 code.

3.1. (eγ)-channel

To study the nature of the background in the source foils, eγ events were examined. Only eγ ''back-to-back'' events (both scintillator arrays fired) were selected in this analysis because time-of-flight criteria cannot distinguish between the Compton effect originating in the scintillators and in the foils when the electron and photon are detected in the same scintillator array.

The external photon flux was the same for both enriched and natural foils of Se and Zr. This was insured by their simultaneous measurement [10] and supported by the findings of a previous experiment with Cd foils [9]. The Zr foils occupied a small central part ($\sim 10\%$) of the source plane. Given a uniform external photon flux the enriched zirconium foil had 10% more eγ events due to its greater mass.

The ''hot'' spot, a spot of radioactive contamination, is readily identified by its high activity in the plot of the eγ vertex distribution (Fig. 2). The activity in a circle of the 1 cm radius centered on the spot ($\sim$ the vertex position resolution) was more than 16 times (40 standard deviations) the mean value of background. To exclude reliably events associated with the ''hot'' spot and the surrounding neighbourhood the region was excluded from the data sample by a cut on the events in a circle of the 3 cm radius centered on the spot. The excluded region reduced the effective enriched zirconium foil by 5.85%. Information on the nature of the pollution was extracted from the γ and eγ energy spectra by fitting contributions of different radioactive nuclei to the spectra. The spectrum shape can be explained with ^{232}Th chain components. After dismounting the source the ''hot'' spot was removed (its mass equals to 1.2 g) and measured by a HPGe

Table 2
Radioactive contaminations in the ''hot'' spot, measured by a HPGe detector and the NEMO-2 detector. The results are given in mBq/kg.

Isotope	HPGe-97	NEMO2 fit
^{208}Tl	160 ± 30(stat)± 16(syst)	72^{+25}_{-20}(stat)± 11(syst)
^{212}Bi	500 ± 120(stat)± 50(syst)	201^{+64}_{-50}(stat)± 31(syst)
^{228}Ac	840 ± 40(stat)± 84(syst)	842^{+67}_{-63}(stat)± 130(syst)

detector. The results presented in Tables 1 and 2 suggest that the ^{232}Th (and/or ^{228}Ra) impurity was introduced to the enriched zirconium foil during the installation of the sources into the NEMO-2 detector. The gradual increase in the decay of ^{228}Th ($T_{1/2} = 1.91$ y) has led to an increase in ^{212}Bi and ^{208}Tl activities during the 10357 h of measurement.

The external background for the zirconium foils was estimated with data from the experiments on ^{82}Se [10] and ^{116}Cd [9]. The eγ events for the cadmium foils, owing to their very low levels of contamination, were assumed to be purely of external origin. Coupling this information with masses, positions and compositions of the selenium and zirconium foils, an energy distribution for the external eγ component was calculated and is shown in Fig. 3. Here the dashed line is the external eγ energy distribution in the zirconium foils. The total number of external eγ events for $E_e + E_\gamma > 0.4$ MeV was 132 ± 17 for the natural zirconium foil and 137 ± 18 for the enriched zirconium foil.

Fitting the eγ energy spectra was done with a number of fixed activities from the HPGe measurement (^{152}Eu, ^{154}Eu and ^{40}K). These results are presented in Table 3 and in Fig. 3.

The fit to the ^{228}Ac activity in the enriched zirconium foil is in a good agreement with the HPGe measurements (Table 1). As to the ^{208}Tl and ^{212}Bi activities the best
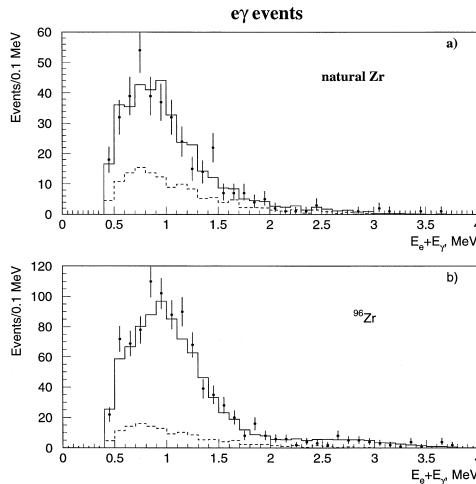

Fig. 3. Energy distributions of eγ events in (a) the natural zirconium foil and (b) in the enriched zirconium foil. Points with error bars are experimental data. The dashed line is the external background estimation. The solid line is the sum of calculated internal and estimated external backgrounds.

Table 3
The radioactive contaminations found by fitting the eγ energy spectra with fixed values from the HPGe measurements (marked by *). Activities are given in mBq/kg.

Isotope	Natural Zr	Enriched Zr
^{208}Tl	$2.0^{+1.3}_{-0.9}$	$15.8^{+3.0}_{-2.7}$
^{212}Bi	$5.5^{+3.6}_{-2.5}$	$43.6^{+8.3}_{-7.5}$
^{214}Bi	$6.6^{+2.9}_{-2.0}$	$10.8^{+2.9}_{-2.4}$
^{228}Ac	$16.5^{+3.2}_{-2.9}$	96 ± 13
^{152}Eu*	204 ± 16	153 ± 21
^{154}Eu*	–	< 36
^{40}K*	–	1133 ± 117

computed fit to the eγ data (Table 3) led to a conclusion similar to the ''hot'' spot. Some ^{232}Th (and/or ^{228}Ra) impurity must have been introduced during the production of the enriched foil. It should be noted that earlier measurements [13,14] with the same enriched ZrO$_2$ powder sample did not find many of the isotopes reported in Table 1 besides ^{40}K. It means that ^{152}Eu, ^{154}Eu, ^{137}Cs were also introduced during the processes of producing the foils and their installation.

3.2. Single electron channel

Single electron events recorded in the NEMO-2 detector were used to estimate activities of single beta emitters such as ^{234m}Pa and ^{90}Y (the daughter of ^{90}Sr), which can contribute to the 2e channel due to the Möller scattering. These emitters have approximately the same beta energy spectra given their nearly equal Q-values (~ 2.3 MeV). Thus, the NEMO-2 detector fails to distinguish between these isotopes. Further,
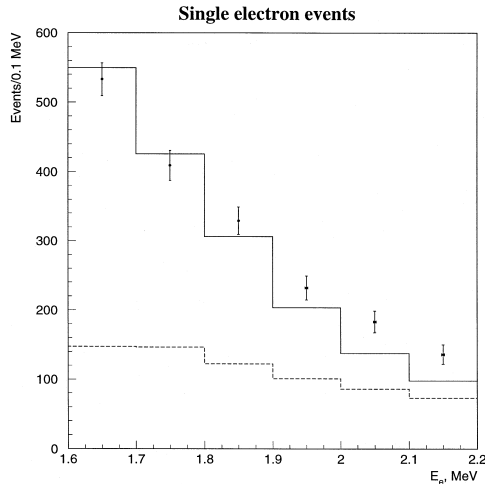

Fig. 4. Single electron energy spectra in the enriched zirconium foil. Points with error bars are experimental data with the internal radioactive impurities removed. The dashed line is the external background. The solid line is the sum of the ^{234m}Pa contribution (84 ± 19 mBq/kg) and external background.

^{234m}Pa is assumed to denominate jointly both isotopes and its activity determined as follows. The single electron energy spectra of the enriched and natural zirconium foils were analysed together in the range $1.6\,\mathrm{MeV} < E_\mathrm{e} < 2.2$ MeV. An excess activity assigned to ^{234m}Pa was found to exist in the enriched zirconium foil at the level of 84 ± 19 mBq/kg (Fig. 4).

4. Results

4.1. $\beta\beta2\nu$ signal of ^{96}Zr

In the first step the 2e events are selected by time-of-flight analysis. The raw data energy spectra in the natural and enriched zirconium foils are shown in Fig. 5. In the energy range 0.40 to 2.4 MeV, which is of interest in $\beta\beta2\nu$, the number of events in each foil was 26 and 114, respectively.

The 2e background in the enriched zirconium foil is calculated by using 2e events in the natural zirconium foil and contamination as measured by the detector itself and a HPGe detector. Table 4 presents contributions to 2e events from different radioactive impurities, external background and $\beta\beta2\nu$ decay of ^{96}Zr.

The external background in the enriched foil is computed from the external background in the natural foil by applying the normalization factor of 1.04 taking into account different masses and the removed ''hot'' spot. This normalization factor used in the case of the eγ analysis is applicable because the increase of the Möller effect is roughly cancelled by the rejection of electrons due to the increase of their energy loss. A 5% error is added to the systematic error because of this approximation.

To improve the signal-to-background ratio the cuts $E_{2\mathrm{e}} > 1.2$ MeV and $\cos(\theta_{\mathrm{ee}}) < 0.6$ were applied to further analysis (Table 4). In this case the external background is close to zero, which is compatible with the previous ^{116}Cd experiment [9] and the signal-to-
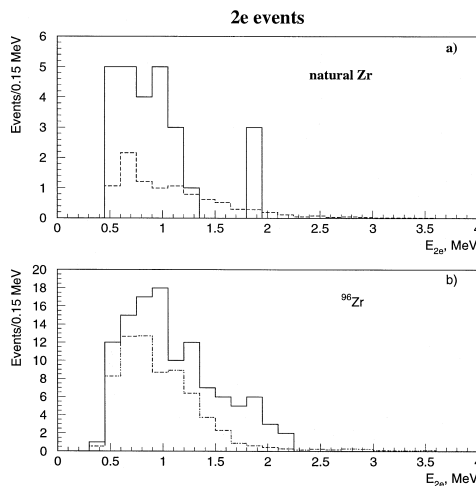

Fig. 5. Summed electron energy spectra of 2e events in (a) the natural zirconium foil and (b) in the enriched zirconium foil. The dashed line represents the internal background contributions.

Table 4
Two electron events in the natural and enriched zirconium foils with estimated contributions of internal impurities, external background and the $\beta\beta$ decay effect

Experiment	26	114	4	41
Nucleus	$E_{2e} > 0.4$ MeV		$E_{2e} > 1.2$ MeV	
	Natural Zr	Enriched Zr	Natural Zr	Enriched Zr
^{234m}Pa	–	14.8 ± 3.4	–	4.0 ± 0.9
^{208}Tl	1.4 ± 0.7	9.1 ± 2.0	0.5 ± 0.3	3.3 ± 0.7
^{212}Bi	0.5 ± 0.3	3.1 ± 0.7	0.1 ± 0.1	0.8 ± 0.2
^{214}Bi	3.4 ± 1.2	5.6 ± 1.4	2.0 ± 0.7	3.3 ± 0.8
^{228}Ac	2.4 ± 0.4	13.3 ± 1.9	0.5 ± 0.1	2.9 ± 0.4
^{152}Eu	2.1 ± 0.2	1.6 ± 0.2	0	0
^{154}Eu	–	0.5 ± 0.5	–	0
^{40}K	–	14.7 ± 1.5	–	0
Int. bkgr	9.8 ± 1.5	62.7 ± 4.9	3.1 ± 0.8	14.3 ± 1.5
Ext. bkgr	14.5 ± 5.4	15.1 ± 5.6	0 ± 2.2	0 ± 2.3
$\beta\beta$ effect	1.7 ± 0.6	36.2 ± 13.7	1.3 ± 0.4	26.7 ± 7.9

background ratio increases from 0.5 for $E_{2e} > 0.4$ MeV to 1.9 for $E_{2e} > 1.2$ MeV. With the cuts applied to the 2e events, the $\beta\beta 2\nu$ detection efficiency equals to 2.99% in the energy range $E_{2e} > 0.4$ MeV and 1.86% for $E_{2e} > 1.2$ MeV.

The $\beta\beta 2\nu$ energy spectrum in the enriched zirconium (Fig. 6) is obtained by subtracting the background spectra from the raw 2e spectrum. This spectrum is fitted to the simulated spectrum in the energy range $E_{2e} > 1.2$ MeV and one gets

$$T_{1/2}^{2\nu} = \left[2.1^{+0.8}_{-0.4}(\text{stat}) \pm 0.2(\text{syst})\right] \cdot 10^{19} \text{ y}.$$

The probability for the background to imitate this effect is less than $5 \cdot 10^{-7}$, or more than five standard deviations above the background level.
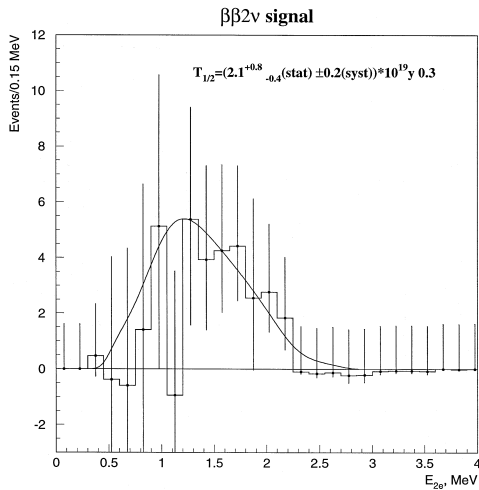

Fig. 6. The experimental $\beta\beta 2\nu$ spectrum of ^{96}Zr. The solid line represents the simulated spectrum with a fit to the half-life $T_{1/2}$ in the energy range $E_{2e} > 1.2$ MeV.
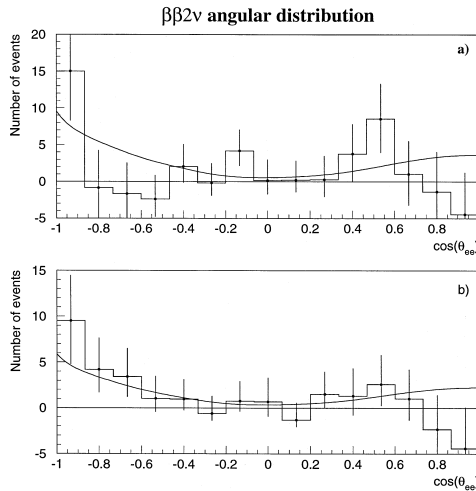
Fig. 7. Angular distribution of $\beta\beta2\nu$ events in ^{96}Zr for (a) $E_{2e} > 0.4$ MeV and (b) for $E_{2e} > 1.2$ MeV. Points with error bars are experimental data and the curve is simulated $\beta\beta2\nu$ events, which corresponds to $T_{1/2} = 2.1 \cdot 10^{19}$ y.

The main contributions to the systematic error quoted above are due to the Monte Carlo calculations, energy calibration, track reconstruction, and internal and external background subtractions. The uncertainty in the Monte Carlo efficiency calculation is estimated to be 3%. The energy calibration error (10 keV for 200 keV electrons) introduces an error of 2.6%. The track reconstruction introduces a 2% uncertainty, and an uncertainty of 5.4% is due to the internal background subtraction of the ^{228}Ac, ^{214}Bi, ^{208}Tl and ^{234m}Pa contributions. Finally, the external background subtraction leads to an error of 5%. Collectively the total systematic error is then 9%.

The angular distribution of $\beta\beta2\nu$ events is presented in Fig. 7. As one can see the deviation from the expected shape of $\beta\beta2\nu$ events, caused by the large background subtraction, decreases for summed electron energies greater than 1.2 MeV. Discrepancies in the calculated and experimental angular spectra for $\cos(\theta_{ee}) > 0.6$ is connected with the large background, which gives a large statistical error.

4.2. $\beta\beta2\nu$ signal of ^{94}Zr

In addition to the ^{96}Zr $\beta\beta2\nu$ signal one can put a direct limit on ^{94}Zr $\beta\beta2\nu$ and $\beta\beta0\nu$ decay modes, because 17.38% of natural Zr is ^{94}Zr ($Q_{\beta\beta} = 1144$ keV). 14 events were detected in the (0.4–0.9) MeV energy interval in the natural Zr foil (see Fig. 5a). Taking into account internal (see Fig. 5a) and external backgrounds we expect 12 background events in this interval. The detection efficiency for the $\beta\beta2\nu$ decay of ^{94}Zr is 10^{-4}. So one can put a limit of

$$T_{1/2}^{2\nu} > 1.1 \cdot 10^{17} \text{ y} \quad (90\% \text{ C.L.}).$$

4.3. Limits on 0ν modes of ^{96}Zr and ^{94}Zr

Monte Carlo simulations of the summed electron energy spectra are shown in Fig. 8 for $\beta\beta0\nu$ decays of ^{96}Zr to the ground state, with and without Majoron emission, and
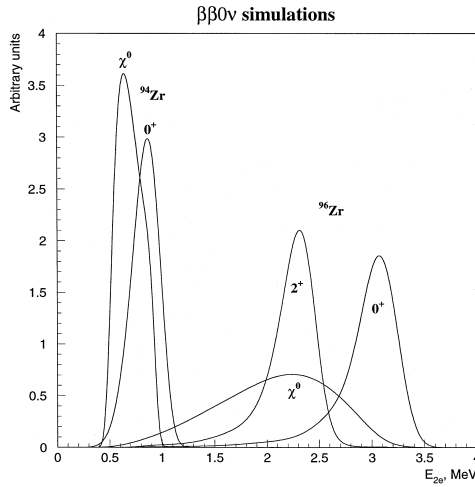
Fig. 8. The simulated $\beta\beta0\nu$ spectra of ^{96}Zr and ^{94}Zr used in computing the corresponding limits.

for decays to the excited 2^+ state (778 keV) of ^{96}Mo, and for $\beta\beta0\nu$ decay of ^{94}Zr to the ground state of ^{94}Mo with and without Majoron emission.

Half-life limits extracted from the data are given in Table 5. The energy windows, number of events, backgrounds, and efficiencies are also given. Limits are computed with the formula for Poisson processes with background [15,16].

4.4. Nuclear matrix element calculation for Majoron emission in ^{96}Zr

The nuclear matrix element involved in the Majoron emission, M_{χ^0}, is obtained from the double Fermi and Gamow–Teller matrix elements in the usual fashion (see e.g. [3]). The relevant matrix elements were calculated using the formalism of [17–19] and the single-particle basis consisting of 10 single-particle orbitals. The same single-particle basis set for protons and neutrons was used. Basically, the single-particle energies were taken from a Coulomb-corrected Woods–Saxon potential but some adjustment of these energies were done near the proton and neutron Fermi energies to obtain a more realistic mean field with respect to the single-quasiparticle energies [20]. The details of this

Table 5
Half-life limits (90% CL). For each decay channel an energy window is defined, the corresponding number of experimental and expected events, the efficiency, and the half-life limit are given

Channel	^{96}Zr			^{94}Zr	
	$0^+_{g.s.}$	Majoron	2^+	$0^+_{g.s.}$	Majoron
Window, MeV	[2.25–3.5]	[2.25–3.5]	[2.25–3.5]	[0.4–1.2]	[0.4–1.2]
Number of events	0	0	0	22	22
Background + $\beta\beta2\nu$	0	0	0	20	20
Efficiency	0.072	0.025	0.027	0.02	0.0024
$T_{1/2}(10^{20}$ y) (90%)	> 10	> 3.5	> 3.9	> 0.19	> 0.023

process have been described in Ref. [21] for the two-neutrino double-beta-decay calculations and here exactly the same basis was used. In the notation of [3] we obtain for the Majoron matrix element $M_{\chi^0} = 5.58$, and using the phase-space factor given in Ref. [3] we obtain for the upper limit of the Majoron–Majorana neutrino coupling constant a value $|\langle g_{\chi^0}\rangle| \leq 2.6 \times 10^{-4}$. The same matrix element was also calculated in the Woods–Saxon basis by Staudt et al. [24]. For their matrix element one obtains the upper limit $|\langle g_{\chi^0}\rangle| \leq 4.9 \times 10^{-4}$.

5. Discussion and conclusion

This is the first direct measurement of the half-life of double-beta decay of ^{96}Zr. The previous value, $T_{1/2} = (3.9 \pm 0.9) \cdot 10^{19}$ y, was obtained from a geochemical experiment [22]. Though it is higher by a factor of ~ 2, the results do not contradict each other given the errors in the measurements[2].

Using the $\beta\beta 2\nu$ half-life presented here and the phase space factor $G = 1.8 \cdot 10^{-17}$ y^{-1} (for the bare axial-vector coupling constant $g_A = 1.254$, [3]), one obtains the nuclear matrix element $M_{2\nu} = 0.051^{+0.007}_{-0.008}$ (scaled by the electron rest mass) or $M_{2\nu} = 0.100^{+0.013}_{-0.016}$ MeV^{-1}. If one wants to use the effective value of the axial-vector coupling constant $g_A = 1.0$, one ends up with the phase-space factor (G scales as g_A^4) $G = 7.3 \cdot 10^{-18}$ y^{-1} and the respective nuclear matrix element values $M_{2\nu} = 0.080^{+0.010}_{-0.013}$ or $M_{2\nu} = 0.157^{+0.020}_{-0.025}$ MeV^{-1}. Theoretical estimations of $M_{2\nu}$ for ^{96}Zr are in the range of 0.034–0.31 for $g_A = 1.254$ [14,24–28]. It should be noted that modern models for nuclear matrix elements calculations have not enough predictable ability and the indefiniteness of the calculations is accepted to count approximately the factor of 2. Nuclear matrix elements calculated within QPRA models has a very strong dependence on the parameter g_{pp} characterizing a particle–particle interaction in a nucleus. Due to that a small change in g_{pp} allows to fit calculated values to experimental ones (see, for example, [25,26]), but it is just a fit. Present status of nuclear matrix calculations are reported in Ref. [3].

The limit on the $\beta\beta 0\nu$ decay of ^{96}Zr obtained in the present work exceeds the best previous one [29] by about two orders of magnitude. Using the nuclear matrix element for the $\beta\beta 0\nu$ decay from [24], one finds the lower limit on the effective Majorana neutrino mass, $\langle m_\nu \rangle < 23$ eV. It should be noted that the limit on the $\beta\beta 0\nu$ decay of ^{96}Zr to the first 2^+ excited state of the daughter nucleus exceeds the earlier value [14] by 5 times.

Limits on 2ν-, 0ν- and $0\nu\chi^0$-$\beta\beta$ processes in ^{94}Zr obtained here also exceed the best previous ones [30] by one or two orders of magnitude.

The zirconium measurements were the last experiments to be carried out with the NEMO-2 detector which has been dismounted. In summary the NEMO-2 detector has

---

[2] If this difference is confirmed then it could be indicative of a time variation of the weak interaction constant, as pointed out in Ref. [23]. Moreover, as a geochemical measurement does not distinguish between different decay modes it gives the total rate of the ^{96}Zr–^{96}Mo transition including single-beta ^{96}Zr–^{96}Nb–^{96}Mo transitions, i.e. the real value of $T^{2\nu}_{1/2}$ from a geochemical experiment can be higher. A ^{96}Zr measurement is planned for the NEMO-3 detector, that will reduce the error to 10% of the current direct measurement.

been highly effective at a number of double beta decay measurements and as a prototype it has provided invaluable experience for the successful operation of NEMO-3. The mounting of NEMO-3 in the Fréjus Underground Laboratory had started in the end of the year 1998 and data collection is foreseen to begin in the beginning of 2000.

Acknowledgements

References

[1] M. Moe, P. Vogel, Ann. Rev. Nucl. Part. Sci. 44 (1994) 247.
[2] H.V. Klapdor-Kleingrothaus, A. Staudt, Non-accelerator Particle Physics (Institute of Physics Publishing, Bristol, PA, 1995).
[3] J. Suhonen, O. Civitarese, Phys. Rep. 300 (1998) 123.
[4] A. Barabash, Proc. First Int. Four Sea Conf., Trieste, Italy, 26 June–1 July 1995, preprint CERN 97-06, p. 176.
[5] NEMO-3 Proposal, LAL preprint 94-29 (1994).
[6] D. Dassié *et al.*, Nucl. Instr. Meth. A 309 (1991) 465.
[7] R. Arnold *et al.*, Nucl. Instr. Meth. A 354 (1995) 338.
[8] D. Dassié *et al.*, Phys. Rev. D 51 (1995) 2090.
[9] R. Arnold *et al.*, Z. Phys. C 72 (1996) 239.
[10] R. Arnold *et al.*, Nucl. Phys. A 636 (1998) 209.
[11] A.S. Barabash, Nucl. Phys. A 629 (1998) 517c.
[12] P. Billoir, Nucl. Instr. Meth. A 255 (1984) 352.
[13] C. Arpesella *et al.*, Europhys. Lett. 27 (1994) 29.
[14] A.S. Barabash *et al.*, J. Phys. G 22 (1996) 487.
[15] O. Helene, Nucl. Instr. Meth. B 212 (1983) 319.
[16] Particle Data Group, Phys. Rev. D 50 (1994) 1281.
[17] J. Suhonen, S.B. Khadkikar, A. Faessler, Phys. Lett. B 237 (1990) 8.
[18] J. Suhonen, S.B. Khadkikar, A. Faessler, Nucl. Phys. A 529 (1991) 727.
[19] J. Suhonen, S.B. Khadkikar, A. Faessler, Nucl. Phys. A 535 (1991) 509.
[20] J. Suhonen, T. Taigel, A. Faessler, Nucl. Phys. A 486 (1988) 91.
[21] M. Aunola, J. Suhonen, Nucl. Phys. A 602 (1996) 133.
[22] A. Kawashima, K. Takahashi, A. Masuda, Phys. Rev. C 47 (1993) 2452.
[23] A.S. Barabash, JETP Lett. 68 (1998) 1.
[24] A. Staudt, K. Muto, H.V. Klapdor-Kleingrothaus, Europhys. Lett. 13 (1990) 31.
[25] S. Stoika, I. Mihut, Nucl. Phys. A 602 (1996) 197.
[26] J. Toivanen, J. Suhonen, Phys. Rev. C 55 (1997) 2314.
[27] O.A. Rumyantsev, M.H. Urin, Phys. Lett. B 443 (1998) 51.
[28] H. Ejiri, H. Toki, J. Phys. Soc. Jpn 65 (1996) 7.
[29] Yu.G. Zdesenko, V.N. Kuts, I.A. Mytsyk, A.S. Nikolaiko, Bull. Ac. Sci. USSR Phys. Ser. 45 (1981) 1856.
[30] A.S. Barabash et al., preprint ITEP 131-90 (1990).